RSC Applied Polymers

ROYAL SOCIETY OF CHEMISTRY

COMMUNICATION

View Article Online
View Journal | View Issue



Cite this: *RSC Appl. Polym.*, 2026, **4**, 200

Received 24th July 2025,
Accepted 1st December 2025

DOI: 10.1039/d5lp00233h

rsc.li/rscapplpolym

# Humidity-driven bilayered composite nanofiber textile actuators for smart heat and humidity management

Xi Yu,[a,c] Qiang Zhou,[a] Yingxin Zhao,[a] Guiying Xu,[a] Peimin Shen,[a] Yang Wang,*[a,c] Chi-wai Kan,*[d] Hui Yu,[a,c] Lihuan Wang,[a,c] Jianhua Yan[a,b] and Xianfeng Wang[a,b]

**The dynamic thermoregulation of skin is often hindered by traditional clothing, leading to discomfort and skin issues. To address this issue, we developed a humidity-responsive bilayered nanofiber textile, combining hydrophilic polyamide (PA) and superhydrophobic polyvinylidene fluoride/fluorinated polyurethane (PVDF/FPU) *via* electrospinning, enabling asymmetric hygroscopic bending up to 165.4° at 100% relative humidity (RH). This enhances moisture permeability (12 602 g $m^{-2}$ $d^{-1}$), 2.8 times higher than that of non-windowed textiles. Reversible water adsorption/desorption enables dynamic actuation for improved sweat evaporation and heat dissipation. This smart textile offers promising applications in sportswear and medical dressings, bridging the gap between static fabrics and dynamic physiological needs.**



As the body's largest interface with the external environment, the skin regulates temperature through sweating and capillary action to maintain thermal balance.[1] However, traditional clothing, serving as a "second skin" covering the body, forms a "skin–clothing–environment" interface that often blocks heat and sweat release, leading to local humidity build-up and discomfort. While strategies like radiative cooling[2,3] and conductive heat dissipation[4] have been proposed for static conditions like specific high-temperature or high-metabolic conditions, they fail to adapt to dynamic environmental changes. Thus, developing smart thermoregulatory textiles with skin-like responsiveness is essential for maintaining wearer comfort under varying environmental conditions.[5,6] Currently, thermoregulatory textiles primarily rely on two mechanisms: (i) unidirectional moisture-wicking fabrics,[7–9] which utilize wettability gradients to facilitate directional liquid sweat transport, and (ii) phase-change thermoregulatory fabrics,[10–14] which leverage the latent heat storage/release properties of phase-change materials to modulate microclimate temperature. However, these approaches exhibit significant limitations when subjected to extreme conditions such as intense physical activities that induce profuse sweating, and existing strategies fail to provide timely thermal relief.[15,16]

An ideal smart textile would autonomously regulate heat and moisture by sensing microclimate conditions—opening breathable "windows" for ventilation under heat and humidity and then closing them to retain body heat after dissipation. To realize this smart window-textile functionality, two key challenges require to be overcome, including humidity-responsive actuation in the material[17] and integration of such functional materials into textile systems. Researchers have developed various bilayered actuation systems based on hydrophilic–hydrophobic heterointerfaces.[18–21] The previously reported dual-layer driven systems primarily employed solution casting, filter deposition, or coating of active materials onto substrates.[22–24] These materials are constrained by their large structural unit size and small specific surface area, which result in a slow response to humidity. Current efforts focus on enhancing interfacial stability, improving responsiveness, and adding functionalities such as conductivity or antibacterial activity for broader wearable applications in smart wearables,[25] soft robotics[26–28] and intelligent packaging.[29,30]

Recent advances in smart window textiles have led to innovative bilayered designs for dynamic thermal and moisture regulation. For example, PA-based textiles with asymmetric origami structures and PPy@MXene coatings exhibit humidity-responsive bending, enhancing sweat evaporation and heat transfer.[31] Similarly, biologically inspired systems combining hygroscopic *Escherichia coli* cells with hydrophobic latex layers enable reversible shape-morphing for ventilated sportswear.[32] These approaches improve moisture control but often rely on composite fiber-coated structures, which limit breathability. In contrast, electrospun nanofiber membranes offer high porosity, excellent air permeability, and interconnected pore networks,[33–35] addressing these limitations. Moreover, electro-

[a]*Guangdong-Hong Kong Joint Laboratory for New Textile Materials, School of Textile Materials and Engineering, Wuyi University, Jiangmen, 529020, China. E-mail: wang.yang@wyu.edu.cn*
[b]*Innovation Center for Textile Science and Technology, Donghua University, Shanghai 200051, China*
[c]*Guangdong Laboratory of Chemistry and Fine Chemical Industry Jieyang Center, Jieyang 515200, China*
[d]*Institute of Textiles & Clothing, The Hong Kong Polytechnic University, Hong Kong 100872, China. E-mail: kan.chi.wai@polyu.edu.hk*

spinning is a versatile and scalable technique with broad material compatibility, making it ideal for fabricating next-generation smart window textiles.[36–38]

In this work, a bilayered nanofiber composite system with reversible humidity-responsive characteristics was constructed through a stepwise electrospinning strategy (Fig. 1a), with its functionality based on the synergistic mechanism between hydrophilic and hydrophobic layers. The fabrication process was specifically designed as follows: a hydrophilic PA nanofiber base membrane was prepared *via* electrospinning. PA was selected as the base membrane material because of the abundant amide bonds (–CONH–) in its molecular chains, which can efficiently capture environmental water molecules through hydrogen bonding. Subsequently, a hydrophobic PVDF/FPU nanofiber membrane with a core–shell structure was deposited *in situ* on the hydrophilic membrane through coaxial electrospinning. A stable interface between the hydrophobic and hydrophilic layers was formed through fiber interlocking and physical interactions such as van der Waals forces, which provided the critical structural foundation for humidity-responsive behavior.

When the bilayered system was exposed to a high-humidity environment (100% RH), water molecules penetrated into the amorphous regions of PA, and the PA layer expanded *via* hydrogen bonding-induced hygroscopic swelling, while the PVDF/FPU layer remained unchanged. This asymmetric strain, constrained by interfacial interactions, drove the film to bend. This bending behavior was reversible, with the driving force originating from the reversible adsorption/desorption of water molecules in PA. Based on this mechanism, the electrospun bilayered nanofiber membrane demonstrated remarkable advantages in intelligent thermo-hygroscopic textiles (Fig. 1b); when the human body sweats under sunlight or during high-intensity exercise, the relative microenvironmental humidity rapidly increases with sweat excreted on the skin, triggering the curling of the bilayered nanofiber membrane. This intelligent response behavior not only facilitates rapid evaporation of sweat but also enhances heat dissipation by increasing the effective skin surface area, achieving dynamic cooling effects.

The microstructural morphology of nanofiber membranes was significantly altered by adjusting the PA concentration (8–20 wt%) in the spinning solution (Fig. 2a–d). At 8 wt% PA concentration, bead-like structures were prevalent in the fiber membrane due to low solution viscosity, which led to jet instability during electrospinning, resulting in a bead-fiber mixed morphology. As the PA concentration increased from 8 to 20 wt%, the viscosity of solution increased, the bead structure gradually disappeared, and the diameter distribution became more uniform. The average nanofiber diameter increased from 447.5 nm to 668 nm. Furthermore, the packing density of fibers was reduced with increased concentration, with the average pore diameter increasing from 0.33 μm to 0.53 μm (Fig. 2e). And these nanofiber membranes all have good moisture permeability due to their interconnected pore structure (Fig. 2f). It is worth noting that the WVT rate of 20 wt% PA membranes was slightly decreased, which may be attributed to the thicker nanofibers leading to a reduction in the porosity.

The wetting properties of PA nanofiber membranes with different concentrations were compared and are presented in Fig. 2g and h. The time of complete wetting progressively increased with increasing PA concentration: from 13 s (8 wt%) to 16.2 s (12 wt%), 16.8 s (16 wt%), and 28 s (20 wt%), indicating that surface wettability gradually decreased. This phenomenon was attributed to the bead structures increasing the surface roughness of membranes. Since PA is intrinsically hydrophilic, enhanced roughness further improved hydrophilicity and accelerated wetting. Mechanical testing (Fig. 2i) demonstrated that under low-concentration spinning conditions, the inhomogeneous PA nanofiber structure and bead

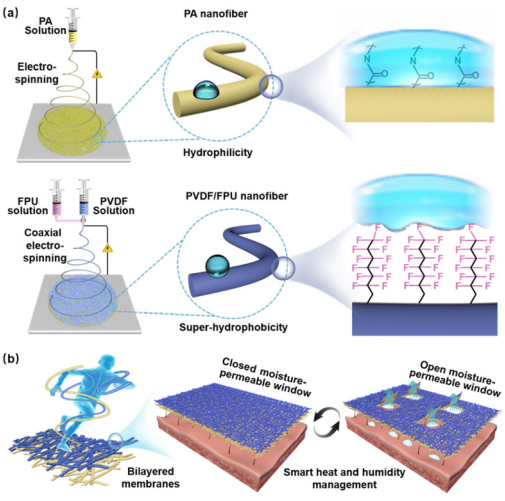


**Fig. 1** (a) Schematic illustration of the fabrication and structure of bilayered membranes. (b) Schematic demonstration of the smart heat-humidity management of bilayered membranes.

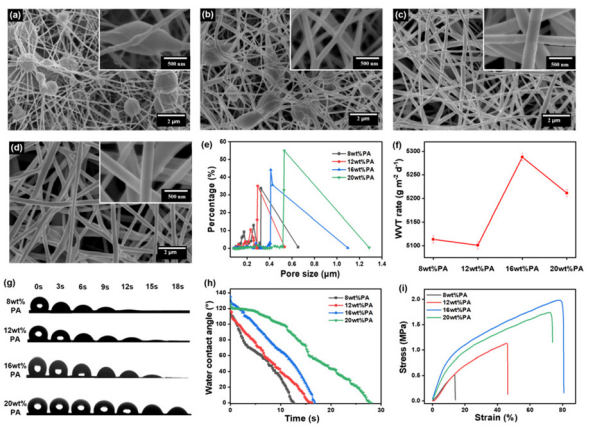


**Fig. 2** SEM images of (a) 8 wt% PA membranes, (b) 12 wt% PA membranes, (c) 16 wt% PA membranes, and (d) 20 wt% PA membranes; (e) pore size distribution, (f) water vapor transmission (WVT) rates, (g–h) water contact angles, and (i) tensile curves of the various PA membranes.

structure-induced stress concentration resulted in a low strength (0.51 MPa) and a low elongation at break (13.75%). At higher concentrations, the PA nanofiber membrane (16 wt%) exhibited significantly improved mechanical properties, with tensile strength and elongation at break reaching 1.98 MPa and 78.8%, respectively. However, with further increasing the concentration to 20 wt%, the mechanical performance was slightly reduced (Fig. 2i), which may have resulted from the increased nanofiber diameter. Based on these results, the 16 wt% PA membrane achieved an optimal balance among moisture permeability, wetting rate, and mechanical properties, and was selected as the base membrane for subsequent bilayered systems.

In this study, polyacrylonitrile (PAN), aramid 1313 (PMIA), PVDF, and PVDF/FPU were selected for the electrospinning fabrication of nanofiber membranes (Fig. 3). Fig. 3a–d show their SEM morphology. Notably, the core–shell PVDF/FPU nanofibers displayed unique nanoscale protrusions resembling the surface morphology of bitter gourd. As shown in Fig. 3g–i, the PVDF/FPU membrane exhibited superior hydrophobic properties, achieving a contact angle of 151.4° and remaining stable for 200 s. The PVDF nanofibers exhibited slightly lower performance with contact angles remaining at 128.8°. To elucidate the difference in their hydrophobic performance, an AFM test was conducted to analyze their structural profiles (Fig. 4a–d and S1, SI). At the single-fiber level, the core–shell 6 wt% PVDF/2 wt% FPU nanofibers displayed nanoscale protrusions (Fig. 4b), and the roughness of the 6 wt% PVDF/2 wt% FPU membranes was apparently higher than that of the 6 wt% PVDF membranes (Fig. 4c). Furthermore, random profile tests conducted on the AFM images showed that the height fluctuation of the 6 wt% PVDF nanofiber was notably smaller than that of the 6 wt% PVDF/2 wt% FPU nanofiber (Fig. 3d), which explains the higher hydrophobicity of the 6 wt% PVDF/2 wt% FPU nanofiber. *In situ* contact angle microscopy further demonstrated that the

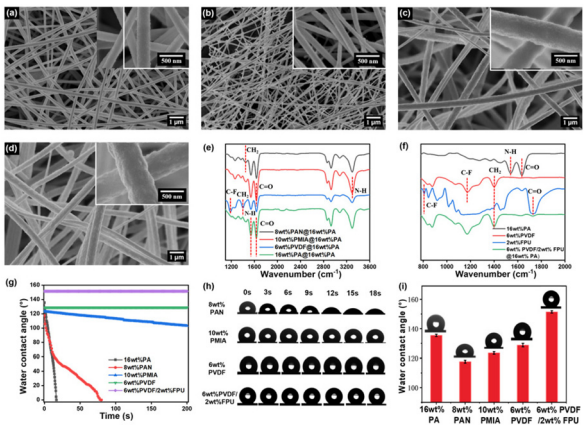


**Fig. 3** SEM images of (a) 8 wt% PAN membranes, (b) 10 wt% PMIA membranes, (c) 6 wt% PVDF membranes, and (d) 6 wt% PVDF/2 wt% FPU membranes; (e and f) FTIR spectra of the various membranes; (g–i) water contact angles of the various membranes.

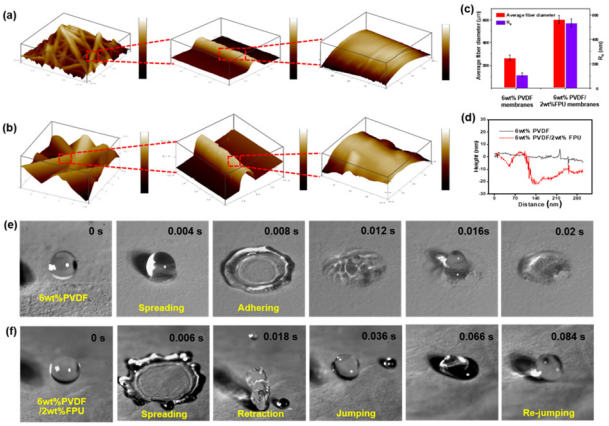


**Fig. 4** 3D AFM images of (a) 6 wt% PVDF and (b) 6 wt% PVDF/2 wt% FPU membranes; (c) average fiber diameters and $R_a$ values; (d) random height curves of 6 wt% PVDF and 6 wt% PVDF/2 wt% FPU membranes; (e–f) snapshots of the impact dynamics for water on the 6 wt% PVDF and 6 wt% PVDF/2 wt% FPU membranes.

nanoscale protrusions on the PVDF/FPU membranes effectively trapped air to form a cushion layer, achieving a superhydrophobic status (Fig. 3g–i).

For fabricating high-performance bilayered nanofiber membranes, we employed *in situ* electrospinning to directly deposit the hydrophobic nanofiber layer onto the 16 wt% PA layer. The resulting bilayered membranes showed stable humidity-responsive actuation and excellent moisture permeability while effectively preventing water/sweat adhesion, maintaining superior moisture-wicking and thermal regulation functionality. As shown in Fig. 3e and f, FTIR analysis confirmed the chemical composition of bilayered membranes. In the spectra of PA/PVDF bilayered membranes, characteristic peaks of PVDF appeared at 1170 $cm^{-1}$ (C–F stretching vibration) and 1402 $cm^{-1}$ ($CH_2$ bending vibration),[39,40] while specific peaks of PA were observed at 1542 $cm^{-1}$ (N–H deformation vibration) and 1630 $cm^{-1}$ (C=O stretching vibration).[41,42] The spectra of the PA/PVDF/FPU bilayered sample additionally revealed the characteristic peaks of FPU at 1720 $cm^{-1}$ (C=O stretching) and 815 $cm^{-1}$ (C–F stretching), confirming the successful incorporation of all three components.[43,44]

Furthermore, a high-speed camera (Fig. 4e and f and Movies S1 and S2, SI) was used to capture dynamic water droplet behaviors. On 6 wt% PVDF membranes, complete wetting occurred within 0.008 s after initial contact (0.004 s spreading), while 6 wt% PVDF/2 wt% FPU membranes exhibited brief spreading (0.006 s), followed by rapid rebound (contact angle >120°) due to their low surface energy. The low surface energy of FPU effectively prevents water adhesion, causing droplets to bounce repeatedly on the material surface without being absorbed. This differential swelling behavior enabled reversible bending responses to humidity changes. Under high humidity conditions (Fig. 5), water molecules penetrated into the amorphous regions of PA layers through fiber interstices, causing hygroscopic expansion, while hydrophobic layers remained dimensionally stable, triggering

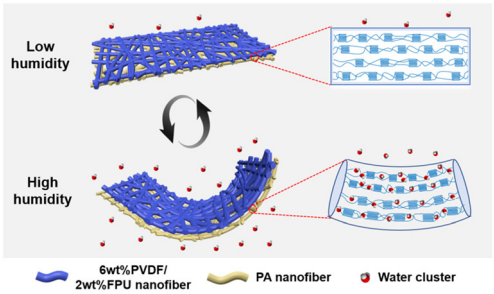


Fig. 5 Schematic demonstration of humidity-responsive bilayered membranes.

bending deformation. When the humidity reduced, water molecules were released from the swelling area, and the bilayered film returned to a straight state from the curved state. The bonding strength between the hydrophilic and hydrophobic layers was crucial for the humidity-responsive functionality of the composite bilayer membrane, and the bilayer composite exhibited good interfacial adhesion property with an average peel strength of 18.2 cN $cm^{-1}$ (Fig. S2, SI).

Quantitative analysis of humidity-responsive actuation (Fig. 6) revealed distinct behaviors among different bilayer combinations, while PA/PVDF and PA/core–shell PVDF/FPU exhibited faster response with maximum bending angles of 120.7° and 165.4°, respectively (Fig. 6a, d and Movies S3–5, SI). All membranes completely recovered to initial states during humidity reduction (from 100% to 40% RH), confirming fully reversible actuation (Fig. 6b). We also designed bilayered membranes with smart windows (trimmed on three sides) to simulate perspiration regulation and evaluate moisture permeability (Fig. S3, SI). The bilayered membrane fabrics with windows could promote human sweat evaporation and cool the body (Fig. S4, SI). Compared to non-windowed samples, the PA/PVDF/FPU system exhibited most pronounced humidity-responsive bending behavior, with a moisture permeability of 12 602 g $m^{-2}$ $d^{-1}$ (Fig. 6c), which was 2.8 and 1.3 times higher than that of non-windowed membranes and PA/PAN windowed membranes, respectively. In addition, the PA/PVDF/FPU bilayered membranes exhibited a two-step fracture process (Fig. S5, SI), indicating that excessive tensile deformation can easily compromise the structural integrity and humidity response function. These results demonstrate excellent adaptive moisture regulation capability, offering new strategies for smart thermoregulatory textiles.

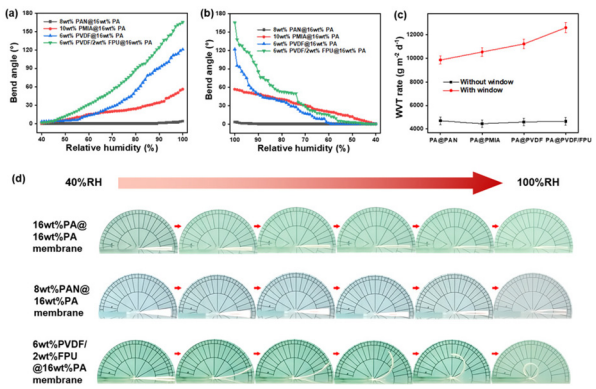


Fig. 6 (a and b) Bend angles of the various bilayered membranes in humidification and dehumidification processes, (c) WVT rates of the various bilayer membranes without windows and with windows, and (d) optical images of the humidity-responsive behavior of the PA/PA membrane, PAN/PA membrane, and PVDF/FPU/PA membrane.

In this study, we developed a humidity-responsive bilayered nanofiber textile for dynamic moisture and heat regulation. When the bilayer nanofiber membrane exhibited distinct differential wettability, it could demonstrate humidity-responsive properties. Using stepwise electrospinning, a hydrophilic PA layer and a superhydrophobic PVDF/FPU layer form a stable structure that bends up to 165.4° at 100% RH, enhancing moisture permeability (12 602 g $m^{-2}$ $d^{-1}$), which is 2.8 times higher than that of non-windowed designs. The bilayered membrane is a promising candidate for smart sportswear and medical dressings for adaptive comfort in changing environments, and also has the potential to be integrated with electronic devices for applications in wearable electronic materials.[45,46]

## Author contributions

Yu Xi: supervision, conceptualization, writing and editing. Qiang Zhou, Yingxin Zhao, Guiying Xu and Peimin Shen: investigation and data curation. Yang Wang and Chi-wai Kan: supervision and writing – review & editing. Hui Yu, Lihuan Wang, Jianhua Yan, and Xianfeng Wang: review & editing.

## Conflicts of interest

There are no conflicts to declare.

## Data availability

The data supporting this article have been included as part of the supplementary information (SI). Supplementary information is available. See DOI: https://doi.org/10.1039/d5lp00233h.

## Acknowledgements

This work was supported by the Key Project of Jiangmen Basic and Applied Basic Research (No. 2320002000907), the Wuyi University Innovation & Entrepreneurship Fund Project (No. 2023CX18), the Science and Technology Special Commissioner Research Project of Jiangmen (No. 2024760000530010383), the High-level Talent Launch Program of Wuyi University (No. 2021AL011 and 2020AL018), the Guangdong/Hong Kong Joint Foundation of Wuyi University (No. 2021WGALH04), and the Foundation of Higher Education of Guangdong, China (No. 2023KCXTD040).

## References

1 J. Vriens, B. Nilius and T. Voets, *Nat. Rev. Neurosci.*, 2014, **15**, 573589.
2 H. Yu, J. Lu, J. Yan, T. Bai, Z. Niu, B. Ye, W. Cheng, D. Wang, S. Huan and G. Han, *Nano-Micro Lett.*, 2025, **17**, 192.
3 R. Wu, C. Sui, T.-H. Chen, Z. Zhou, Q. Li, G. Yan, Y. Han, J. Liang, P.-J. Hung, E. Luo, D. V. Talapin and P.-C. Hsu, *Science*, 2024, **384**, 1203–1212.
4 X. Yu, Y. Li, X. Wang, Y. Si, J. Yu and B. Ding, *ACS Appl. Mater. Interfaces*, 2020, **12**, 32078–32089.
5 N. N. Schommer and R. L. Gallo, *Trends Microbiol.*, 2013, **21**, 660–668.
6 H. Cui, Y. Li, X. Zhao, X. Yin, J. Yu and B. Ding, *Compos. Commun.*, 2017, **6**, 63–67.
7 L. Gao, Y. Bao, P. Lei, S. Yu, X. Zhu, C. Liu, W. Zhang and J. Ma, *J. Mater. Chem. A*, 2024, **12**, 27478–27490.
8 Y. Si, S. Shi, Z. Dong, H. Wu, F. Sun, J. Yang and J. Hu, *Adv. Fiber Mater.*, 2023, **5**, 138–153.
9 W. Fan, G. Zhang, X. Zhang, K. Dong, X. Liang, W. Chen, L. Yu and Y. Zhang, *Small*, 2022, **18**, 2107150.
10 H. Liu, F. Zhou, X. Shi, K. Sun, Y. Kou, P. Das, Y. Li, X. Zhang, S. Mateti, Y. Chen, Z.-S. Wu and Q. Shi, *Nano-Micro Lett.*, 2023, **15**, 29.
11 J. I. So, C. S. Lee, B. S. Kim, H. W. Jeong, J. S. Seo, S. H. Baeck, S. E. Shim and Y. Qian, *Polymers*, 2023, **15**, 1300.
12 Q. Li, X. Huang, H. Liu, S. Shang, Z. Song and J. Song, *ACS Sustain. Chem. Eng.*, 2017, **5**, 10002–10010.
13 C. Ma, Y. Gao, Y. Cao, Y. Yang, W. Wang and J. Wang, *Nano Energy*, 2024, **123**, 109400.
14 X. Yu, Y. Li, X. Yin, X. Wang, Y. Han, Y. Si, J. Yu and B. Ding, *ACS Appl. Mater. Interfaces*, 2019, **11**, 39324–39333.
15 Z. Hou, X. Liu, M. Tian, X. Zhang, L. Qiu, T. Fan and J. Miao, *J. Mater. Chem. A*, 2023, **11**(33), 17336–17372.
16 Y. He, S. Guo, L. Qu, X. Zhang, T. Fan and J. Miao, *Adv. Funct. Mater.*, 2025, 2419923.
17 D. Jiao, Q. L. Zhu, C. Y. Li, Q. Zheng and Z. L. Wu, *Acc. Chem. Res.*, 2022, **55**, 1533–1545.
18 Y. Ge, R. Cao, S. Ye, Z. Chen, Z. Zhu, Y. Tu, D. Ge and X. Yang, *Chem. Commun.*, 2018, **54**, 3126–3129.
19 F. Wu, X. Lin, Y. Xu, Y. Chen, Y. He, J. Wang and M. Liu, *Compos. Sci. Technol.*, 2023, **241**, 110106.
20 L. Yao, J. Ou, G. Wang, C.-Y. Cheng, W. Wang, H. Steiner and H. Ishii, *3D Print. Addit. Manuf.*, 2015, **2**, 168–179.
21 M. Chen, J. Frueh, D. Wang, X. Lin, H. Xie and Q. He, *Sci. Rep.*, 2017, **7**, 769.
22 F. Wu, X. Lin, Y. Xu, Y. Chen, Y. He, J. Wang and M. Liu, *Compos. Sci. Technol.*, 2023, **241**, 110106.
23 X. Li, B. Ma, J. Dai, C. Sui, D. Pande, D. Smith, L. Brinson and P. Hsu, *Sci. Adv.*, 2021, **7**(51), eabj7906.
24 M. Amjadi and M. Sitti, *ACS Nano*, 2016, **10**(11), 10202–10210.
25 J. Wei, S. Jia, J. Wei, C. Ma and Z. Shao, *ACS Appl. Mater. Interfaces*, 2021, **13**, 38700–38711.
26 Y. Zhang, X. Zhou, L. Liu, S. Wang, Y. Zhang, M. Wu, Z. Lu, Z. Ming, J. Tao and J. Xiong, *Adv. Mater.*, 2024, **36**, 2404696.
27 X. Yang, L. Lan, X. Pan, Q. Di, X. Liu, L. Li, P. Naumov and H. Zhang, *Nat. Commun.*, 2023, **14**, 2287.
28 G. Tang, S. Liu, X. Yu, D. Mei, X. Zhao, C. Zhao, L. Li and Y. Wang, *Chem. Engineer. J.*, 2025, **511**, 162057.
29 E. Xue, B. Tian, Y. Wu, Q. Liu, P. Guo, K. Zheng, J. Liang and W. Wu, *ACS Appl. Poly. Mater.*, 2023, **5**, 4525–4535.
30 Q. Chen, B. Sochor, A. Chumakov, M. Betker, N. M. Ulrich, M. E. Toimil-Molares, K. Gordeyeva, L. D. Söderberg and S. V. Roth, *Adv. Funct. Mater.*, 2022, **32**, 2208074.
31 C. Lan, M. Liang, J. Meng, Q. Mao, W. Ma, M. Li and X. Pu, *ACS Nano*, 2025, **19**, 8294–8302.
32 Q. Qi, J. Qian, X. Tan, J. Zhang, L. Wang, B. Xu, B. Zou and W. Tian, *Adv. Funct. Mater.*, 2015, **25**, 4005–4010.
33 Y. He, S. Guo, X. Zhang, L. Qu, T. Fan and J. Miao, *J. Mater. Chem. A*, 2024, **12**(44), 30121–30168.
34 L. Zhou, D. Zhang, X. Ji, H. Zhang, Y. Wu, C. Yang, Z. Xu and R. Mao, *Nano Energy*, 2024, **129**, 109985.
35 Y. Wu, D. Zhang, Y. Zhang, H. Zhang, L. Zhou, Y. Liu, W. Liu and Z. Ding, *Nano Energy*, 2025, 111207.
36 D. Wang, D. Zhang, M. Tang, H. Zhang, F. Chen, T. Wang, Z. Li and P. Zhao, *Chem. Eng. J.*, 2022, **446**, 136914.
37 D. Wang, D. Zhang, P. Li, Z. Yang, Q. Mi and L. Yu, *Nano-Micro Lett.*, 2021, **13**(1), 57.
38 H. Zhang, X. Zhang, C. Qiu, P. Jia, F. An, L. Zhou, L. Zhu and D. Zhang, *Chem. Eng. J.*, 2024, **496**, 154226.
39 M. Ghori, H. Khan, I. Muneer, A. Ali, T. Abbas and H. Bashrat, *Pak. J. Sci.*, 2025, **77**(2), 227–233.
40 W. Kong, Y. Yang, Z. Liu and J. Lei, *J. Polym. Res.*, 2017, **24**(10), 168.
41 M. Lin, F. Chuang, Y. Shu and W. Tsen, *Polym. Plast. Technol. Eng.*, 1998, **37**(1), 71–102.
42 Z. Li, Z. Wang, Y. Zhang, Z. Guo, B. Zhao and S. Liu, *J. Appl. Polym. Sci.*, 2025, **142**(26), e57092.
43 M. Ghori and H. Khan, *Pak. J. Sci.*, 2025, **77**(2), 227–233.
44 N. Li, F. Zeng, Y. Wang, D. Qu, C. Zhang, J. Li, J. Huo and Y. Bai, *Chin. J. Polym. Sci.*, 2018, **36**(1), 85–97.
45 Z. Hou, Y. He, L. Qu, X. Zhang, T. Fan and J. Miao, *Nano Lett.*, 2024, **24**(47), 15142–15150.
46 Y. He, S. Guo, X. Zuo, M. Tian, X. Zhang, L. Qu and J. Miao, *ACS Appl. Mater. Interfaces*, 2024, **16**(43), 59358–59369.